Pulse propagation and electron acceleration in a corrugated plasma channel

J. P. Palastro, T. M. Antonsen, and S. Morshed
Institute for Research in Electronics and Applied Physics, University of Maryland, College Park, Maryland 20742, USA

A. G. York and H. M. Milchberg
Institute for Physical Science and Technology, University of Maryland, College Park, Maryland 20742, USA

(Received 5 December 2007; published 12 March 2008)

A preformed plasma channel provides a guiding structure for laser pulses unbound by the intensity thresholds of standard waveguides. The recently realized corrugated plasma channel [Layer *et al.*, Phys. Rev. Lett. **99**, 035001 (2007)] allows for the guiding of laser pulses with subluminal spatial harmonics. These spatial harmonics can be phase matched to high energy electrons, making the corrugated plasma channel ideal for the acceleration of electrons. We present a simple analytic model of pulse propagation in a corrugated plasma channel and examine the laser-electron beam interaction. Simulations show accelerating gradients of several hundred MeV/cm for laser powers much lower than required by standard laser wakefield schemes.

DOI: 10.1103/PhysRevE.77.036405 PACS number(s): 52.38.Kd, 52.20.Dq, 52.38.−r, 52.35.Mw

I. INTRODUCTION

Preformed plasma channels allow for the propagation of high intensity short laser pulses over distances unrestrained by vacuum diffraction and intensities unlimited by dielectric breakdown. These properties make the preformed plasma channel ideal for applications that rely on long interaction lengths for efficient operation, including x-ray lasers [1], harmonic generation [2], and laser wakefield accelerators [3–9]. In particular, laser wakefield acceleration of electrons offers a promising alternative to conventional RF accelerators and has already produced beams of electrons at GeV in only several centimeters [10]—a gradient three orders of magnitude higher than the Stanford Linear Accelerator. Wakefield acceleration, however, typically requires very expensive multi-terawatt laser systems. These laser systems fail to fit on conventional laser tables, making wakefield accelerated electron beams inaccessible to smaller labs and unrealistic for use in small scale applications.

Direct laser acceleration of electrons has been proposed as a lower power alternative to laser wakefield acceleration. Laser wakefield acceleration relies on the nonlinear ponderomotive force of the laser pulse to generate an electrostatic wave that accelerates the electrons. As a result, the accelerating gradient is quadratic in the laser amplitude. In direct laser acceleration, the laser field itself accelerates the electrons; the accelerating gradient is linear in the laser field amplitude. This linearity allows for a direct laser acceleration scheme that could potentially outperform laser wakefield acceleration.

Direct acceleration is, however, limited by the Lawson-Woodward theorem (LWT) which states: the energy gain of an electron traveling at nearly the speed of light accelerated by a laser pulse in vacuum over an infinite distance is zero [11,12]. Each direct acceleration scheme has thus focused on overcoming one of the underlying assumptions of this theorem to achieve net energy gain. The inverse Cherenkov accelerator was one of the first experiments to demonstrate net energy gain via direct electron acceleration [13]. The observed accelerating gradient of 31 MeV/m (the maximum energy gain was a few MeV), although modest compared to wakefield gradients, provided proof of principle for direct acceleration. The experiment consisted of radially polarized laser light pulse passed through an axicon lens incident on a gas cell at the Cherenkov angle. The electron beam propagated along the axis of the gas cell. The presence of the gas cell overcomes the vacuum assumption of the LWT. In particular, the presence of the dielectric lowered the phase velocity of the laser light, allowing for phase matching with the electron beam over the length of the gas cell. The dielectric that allows for direct acceleration in the inverse Cherenkov accelerator also presents its limitation. For larger laser intensities ($\sim 1\times 10^{14}$ W/cm^2), which can provide more competitive gradients, dielectric breakdown of the gas occurs. The phase velocity of the laser light in the resulting plasma is superluminal precluding phase matching.

Direct acceleration has also been demonstrated in the semi-infinite vacuum scheme [14,15]. For a proof of principle experiment, the peak acceleration was found to be 40 MeV/m comparable to inverse Cherenkov radiation, but maximum energy gains were only on the order of tens of keV. The semi-infinite vacuum accelerator uses linearly polarized laser light incident at an angle to the propagation axis of a relativistic electron beam. The projection of the electric field onto the electron beam propagation axis provides the accelerating gradient. The interaction length is terminated after a finite length by the presence of a gold plated dielectric. The presence of the terminating boundary allows a population of properly phased electrons to gain energy, breaking the symmetry of equal phasing and dephasing periods over an infinite interaction length predicted by the LWT. Because the electron beam is never properly phase matched to the laser light, extending the interaction length will not result in larger maximum energies as with wakefield and inverse Cherenkov accelerators. Furthermore, in the experiments, the incident angle of the laser beam with the electron beam was small ($\sim$16 mrad). The amplitude of the electric field projected onto the electron propagation is thus significantly lower than its peak value.

The vacuum beat wave accelerator has been proposed as a two laser method for direct electron acceleration [16,17]. The

scheme utilizes the laser beams' magnetic forces to achieve acceleration, which are neglected in the LWT. The accelerator involves copropagating two circularly polarized beams each at a different frequency with a relativistic electron beam. The beating of the two laser beams via the $\vec{v}\times\vec{B}$ force on the electrons results in an axially directed ponderomotive force that accelerates the electron beam. The phase velocity of the beat wave can be subluminal and hence matched to the electron velocity. Limitations on the interaction length arise, however, due to the vacuum diffraction of the laser light.

The use of plasma waveguides for direct electromagnetic acceleration has been previously suggested by Serafim *et al.* [18], who proposed guiding a radially polarized laser pulse to accelerate a copropagating relativistic electron beam. For a parabolic plasma density profile, the pulse guides as a transverse magnetic mode. The radial component E_r is a hollow mode with a peak intensity at $r=w_{ch}/\sqrt{2}$, where the channel radius w_{ch} is given by $w_{ch}=(2c)^{1/2}(2/\omega''^2_{p,0})^{1/4}$ and $\omega''^2_{p,0}$ is the second spatial derivative of the plasma frequency. The accelerating field is the associated axial component E_z, which is smaller by a factor of $\sim\lambda/w_{ch}$, where λ is the laser wavelength. The axial electric field peaks at $r=0$ and passes through zero at $r=w_{ch}$. The magnetic field B_θ is purely in the azimuth and has the same radial profile as E_r. Following Ref. [18], the peak axial acceleration gradient from hollow mode guiding in a plasma channel is given by $E_z[\mathrm{GeV/cm}]=0.1\lambda P^{1/2}/w_{ch}^2$ [$\mathrm{W}^{1/2}$ m^{-1}], where P is the peak laser power in W. For a 1 TW laser pulse with $\lambda=800$ nm in a channel supporting $w_{ch}=15$ μm, E_z is an impressive $\sim$30 GeV/m. If the interaction length is long enough (which determines the total energy gain), this could compare favorably to laser wakefield accelerators and at much lower power: Malka *et al.* used a 30 TW laser to produce an acceleration gradient of $\sim$70 GeV/m (200 MeV over 3 mm) [19].

Serafim *et al.*'s scaling also suggests that for long enough interaction lengths direct acceleration in the plasma waveguide could outperform the aforementioned direct acceleration schemes. The plasma waveguide overcomes three limitations of these methods. By using a plasma instead of neutral gas, there is no limitation on the intensity of the accelerating laser as with the inverse Cherenkov accelerator. The natural axial field arising from the propagation of a radial polarized electric field eliminates the need for using the projection of the linearly polarized field as in the semi-infinite vacuum accelerator. A plasma channel with a negative radial gradient in the index of refraction (positive gradient in the plasma density) provides total internal reflections of the laser, eliminating diffraction—the limitation of the vacuum beat wave accelerator.

Extending the interaction length in the plasma waveguide is, however, a problem. The phase velocity of the laser is superluminal and the axial accelerating electric field cannot be phase matched to an electron beam. An electron traveling at nearly c would slip 2π out of phase with the accelerating field after traveling a dephasing length $L_d=\lambda(n_0/n_{cr}+2\lambda^2/\pi^2 w_{ch}^2)^{-1}$, where n_0 is the on-axis electron plasma density of the channel and n_{cr} is the critical plasma electron density for wavelength λ [20]. The electron gains no net energy: it would accelerate for a distance $L_d/2$, and then decelerate an equal amount over the next $L_d/2$.

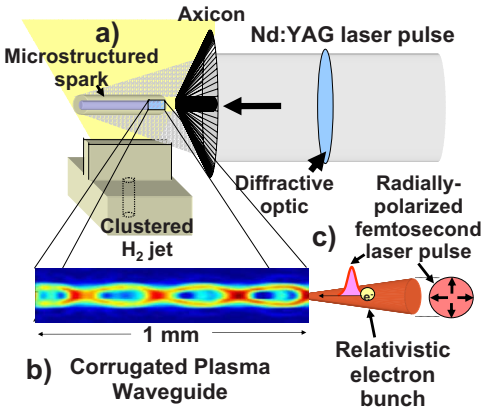

FIG. 1. (Color online) Proposed setup for direct acceleration of electrons by a femtosecond laser pulse in a corrugated plasma waveguide. (a) A radially modulated Nd:YAG laser pulse focused by an axicon onto a gas jet creates a spark several centimeters long with micron-scale structure. The spark expands into (b) a plasma waveguide with axial modulations, allowing fine velocity control of guided radiation [15]. (c) A radially polarized femtosecond laser pulse and a relativistic electron beam are injected into this waveguide.

The experimentally created corrugated plasma waveguide shown in Fig. 1 could *quasi*phase match the laser and electron beam [21]. This can be viewed in two ways. The axially periodic plasma density provides a local phase velocity that is faster in regions of high density and slower in regions of low density. If the laser-electron dephasing length L_d and the corrugation period are matched, the symmetry between acceleration and deceleration in a dephasing cycle is broken, and a properly phased electron will gain net energy; this process can be viewed as the inverse of transition radiation [22]. Alternatively, the guided mode can be viewed as a composition of Fourier spatial harmonics due to the presence of the axially periodic density. For the proper corrugation period, the phase velocity of the spatial harmonics is subluminal, and can be matched to the electron beam velocity. Matching the corrugation period to the laser-electron dephasing length L_d is equivalent to matching the phase velocity of a spatial harmonic to the electron velocity.

The goal of this paper is to examine laser pulse propagation and electron beam dynamics in the corrugated plasma waveguide and to demonstrate that large gradients ($\sim$10 GeV/m) over long interaction lengths ($\sim$2 cm) are possible. In Sec. II we present an analytic model for pulse propagation that provides insight into the field structure inside a corrugated plasma waveguide. The pulse propagation is examined using the slowly varying envelope approximation. The electron density profile used models the one shown in Fig. 1, and allows for an analytic solution to the wave equation. With the field solution, we derive a scaling law for electron energy gain, and compare it to wakefield acceleration and other direct acceleration schemes in Sec. III. Section IV includes calculations and analysis of fully relativistic electron trajectories in the laser electromagnetic field. The calculations are also used to validate the scaling law. Section V contains the conclusions.

II. LASER PULSE PROPAGATION IN A CORRUGATED PLASMA WAVEGUIDE

We start with the radial component of the laser vector potential as follows:

$$A_\perp = \hat{A}_r(r,z,t)\exp[i(k_0 z - \omega_0 t)] + \text{c.c.}, \quad (1)$$

where k_0 and ω_0 are the central wave number and frequency of the laser pulse, respectively. We assume the pulse remains azimuthally symmetric for all time, and consider corrugated plasma channels that have sufficiently low electron densities such that the plasma frequency satisfies $\omega_p \ll \omega_0$, where $\omega_p^2 = 4\pi e^2 n_e(r,z)/m_e$, e is the electron charge, m_e is the electron mass, and n_e is the electron density. In this regime the envelope $\hat{A}_r$ evolves on the time scale ω_0/ω_p^2, which is much longer than the laser period, $2\pi/\omega_0$. The slowly varying envelope equation then determines the evolution of the laser pulse as follows:

$$\left[2ik_0\left(\frac{\partial}{\partial z} + \frac{1}{c}\frac{\partial}{\partial t}\right) + \frac{1}{r}\frac{\partial}{\partial r}r\frac{\partial}{\partial r} - \frac{1}{r^2}\right]\hat{A}_r = \frac{\omega_p^2(r,z)}{c^2}\hat{A}_r, \quad (2)$$

where $\omega_0 = k_0 c$, and we have assumed that the electron plasma responds linearly and as a nonrelativistic cold fluid. We will examine the validity of this assumption in Appendix A. The r^{-2} term in Eq. (2) arises from the cylindrical symmetry of the problem. For solutions of Eq. (2) the appropriate boundary condition at the origin is $\hat{A}_r(r=0,z,t)=0$. To determine the boundary condition at $r=\infty$ we must consider the electron density profile $n_e(r,z)$. For cases of interest, the plasma channel effectively guides the laser pulse and we may consider $\hat{A}_r(r\to\infty,z,t)=0$.

Because the laser-electron dephasing length L_d depends on the electron's velocity, acceleration of subrelativistic electrons would require a structure with either a graded modulation period or an axial taper of the electron density to ensure that the electron remained phase matched to the laser over the entire interaction length. For mathematical simplicity we consider a fixed modulation period and an axially uniform background density, suited to acceleration of electrons with $\gamma \gg 1$ for which the relativistic electron velocity depends only weakly on gamma and L_d is nearly constant. We limit our analysis to a periodic electron density profile that models Fig. 1,

$$n_e(r,z) = n_0[1 + \delta\sin(k_m z)] + n_0'' r^2/2, \quad (3)$$

where δ is the relative amplitude of the density modulation, n_0'' determines the radial dependence, and k_m is the wave number describing the axial periodicity of the channel. For large radii the solution to Eq. (2) is evanescent as the local transverse wave number, $(ck_\perp) \sim \sqrt{\omega^2 - \omega_p^2(r,z) - (ck_z)^2}$, necessarily passes through zero at some radius, and becomes purely imaginary. This is consistent with our boundary condition, $\hat{A}_r(r\to\infty,z,t)=0$, or equivalently the density profile is taken to be lossless. In Appendix B we examine the loss of pulse power from a leaky channel and provide a condition for which the lossless density profile is valid.

The radial dependence n_0'' can also be modulated, but can lead to unstable oscillations in the laser spot size as demonstrated in Appendix C and discussed in Ref. [23]. These oscillations can lead to significant leakage of pulse power from a plasma channel, which cannot be captured by our present analytic model. Furthermore, exact solutions to Eq. (2) with the density profile in Eq. (3) exist, which will simplify analysis of the electron beam dynamics. In arriving at Eq. (2) we have chosen a gauge in which the electrostatic potential $\Phi = 0$. Using this gauge and the fact that $\vec{\nabla}\cdot\vec{E} \simeq 0$ to order $\sim(\omega_p/\omega)^2$, we have that $\vec{\nabla}\cdot\vec{A} \simeq 0$. Thus once A_r has been determined, A_z and the axial electric field can be determined by the condition $\vec{\nabla}\cdot\vec{A}=0$.

The slowly varying envelope approximation neglects second derivatives in z and t in the wave equation, which are responsible for a subluminal group velocity. However, the group velocity can be explicitly restored by replacing $c^{-1}\partial/\partial t$ with $v_g^{-1}\partial/\partial t$ in Eq. (2). Here $v_g/c = 1 - \omega_{p,0}^2/2\omega^2 - 4/(k_0 w_{ch})^2$, and we define $\omega_{p,0}^2 = \langle\omega_p^2(0,z)\rangle_z$, where the brackets represent an average over z and $w_{ch} = (2c)^{1/2}(2/\omega_{p,0}''^2)^{1/4}$ is the width of the guided mode. We note that the group velocity is strictly subluminal due to the presence of the background plasma and guiding channel.

The lowest eigenmode solution of Eq. (2) is

$$\hat{A}_r(r,z,t) = A_0\frac{r}{w_{ch}}e^{-r^2/w_{ch}^2 - (z - v_g t)^2/\sigma_z^2}\sum_n i^n J_n(\psi)e^{-i\psi + i(\delta k + nk_m)z}, \quad (4)$$

where $J_n(\psi)$ is the nth-order Bessel function of the first kind, $\psi = \delta\omega_{p,0}^2/2c^2 k_0 k_m$, and $\delta k = -k_0^{-1}(\omega_{p,0}^2/2c^2 + 4/w_{ch}^2)$. We take the pulse to have a Gaussian temporal shape with duration σ_z/v_g. In Eq. (4), the laser pulse is written as a sum of spatial harmonics. The harmonics have a relative amplitude given by $J_n(\psi)$. For our experimental conditions of $(\omega_{p,0}/\omega_0)^2(k_0/k_m) \ll 1$, $\psi << 1$, and $J_n(\psi) \sim \psi^n/2^n n!$. For small ψ the relative amplitude drops rapidly with increasing harmonic number. Thus only the first few spatial harmonics contribute to the electromagnetic field structure in the corrugated plasma waveguide. This is seen in Fig. 2(a), which shows the relative amplitude for $n=0,1,2,3$ spatial harmonics as a function of ψ.

By forming the ratio of ω_0 to k, and using the fact that $|k_0| \gg |nk_m|, |\delta k|$, we obtain the effective phase velocity $v_{p,n}$ for the nth spatial harmonic as follows:

$$\frac{v_{p,n}}{c} \simeq 1 - \frac{nk_m}{k_0} + \frac{\omega_{p,0}^2}{2\omega^2} + \frac{4}{(k_0 w_{ch})^2}. \quad (5)$$

It should be mentioned that for very large values of n, $|k_0| \gg |nk_m|$ is no longer valid, but as demonstrated above the amplitude of these modes is negligible. The last two terms in Eq. (5) are responsible for the superluminal phase velocity in uncorrugated plasma channels. The second term, due to the axial periodicity of plasma, allows for subluminal phase velocities. The condition for subluminal phase velocity can then be expressed in terms of the laser and channel parameters: $nk_m > k_0[\omega_p^2/2\omega^2 + 4/(k_0 w_{ch})^2]$. Figure 2(b) depicts the

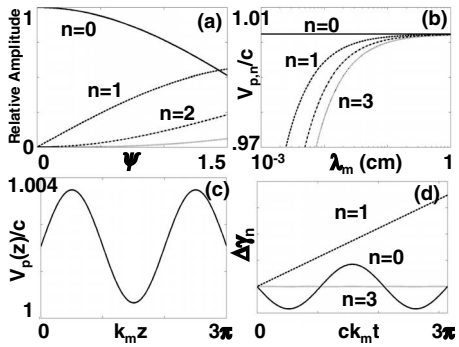

FIG. 2. (a) The relative amplitude of the spatial harmonics as a function of the phase modulation amplitude. (b) The phase velocity for different spatial harmonics as a function of modulation wavelength. (c) The local laser phase velocity as a function of axial distance. (d) Energy contribution of different spatial harmonics for an electron initially phase matched to the $n=1$ spatial harmonic.

phase velocity of the $n=0,1,2,3$ spatial harmonics as a function modulation period for experimental parameters used in Ref. [21]. As expected the funadamental laser mode ($n=0$) is strictly superluminal. The $n=1$ spatial harmonic becomes subluminal for modulation periods of $\sim 300\ \mu$m; modulations of a similar period have been created in experiments [21], which is promising for future experiments on direct acceleration.

The local nature of the laser phase velocity is apparent upon rewriting the sum in Eq. (4) as follows:

$$\sum_n i^n J_n(\psi)\exp[ink_m z] = \exp[i\psi\cos(k_m z)]. \tag{6}$$

We find the local wave number by taking the gradient of $(k_0+\delta k)z-\psi+\psi\cos(k_m z)$. The local phase velocity of the guided mode is then

$$\frac{v_p(z)}{c} \simeq 1 + \frac{\omega_{p,0}^2}{2\omega^2}[1+\delta\sin(k_m z)] + \frac{4}{(k_0 w_{ch})^2}. \tag{7}$$

In regions of high density, $k_m z=\pi(1/2+2\ell)$, where ℓ is an integer, the phase velocity is a maximum, and in regions of low density $k_m z=\pi(3/2+2\ell)$ the phase velocity is a minimum. The difference in local phase velocity between peak and minimum density is $\Delta v_p=\delta(\omega_p/\omega)^2$. Figure 2(c) shows the local phase velocity as a function of axial distance. We note that the local phase velocity is always superluminal. Equation (6) also demonstrates that the spatial harmonics of the guided mode are a result of periodic phase modulations in the laser due to the axial periodic plasma density. Furthermore, the relative amplitude of the spatial harmonics is determined by the amplitude of the phase modulation ψ.

III. SCALING LAW AND COMPARISON TO OTHER SCHEMES

With an analytic expression for the electromagnetic field in the corrugated plasma waveguide, a scaling law for the electron energy gain via quasi-phase-matched direct acceleration can be derived. We start with the expression for the energy gain of an electron in an electric field

$$\Delta\gamma = -\frac{q}{m_e c^3}\int \vec{v}\cdot\frac{\partial\vec{A}}{\partial t}dt, \tag{8}$$

where $\gamma=\sqrt{1+|\vec{p}/m_e c|^2}$. We consider an electron with initial conditions $(r,v_r)=(0,0)$, and $(z,v_z)=(z_0,v_{z,0})$, where $v_{z,0}$ is assumed to be close enough to c such that $(1-v_z/c)\omega_0 t \ll 1$ over the process of acceleration; the electron energy is high enough such that γ depends weakly on velocity, and phase slippage due to acceleration can be neglected. Recalling that the axial electric field provides the acceleration, we have

$$\Delta\gamma = -2\frac{q\omega}{m_e c^2}\,\mathrm{Re}\left[\int iA_z dt\right]. \tag{9}$$

The $n=1$ spatial harmonic is chosen to be phase matched to the electron because it is the largest amplitude mode that also supports a subluminal phase velocity. For phase matching, the phase velocity of the $n=1$ spatial harmonic is set to c, which can be accomplished experimentally by adjusting the corrugation period or density: $k_m=k_0[\omega_p^2/2\omega^2+4/(k_0 w_{ch})^2]$. Although the electron has been phase matched to the $n=1$ spatial harmonic, every spatial harmonic contributes to the energy change of the electron. Upon inserting the axial vector potential into Eq. (9), we find the energy contribution of each spatial harmonic to scale as $\Delta\gamma_n \sim J_n(\psi)\sin[ck_m(n-1)t]/(n-1)$. The contribution from all the harmonics is oscillatory except for the phase matched $n=1$ harmonic, which provides linear energy gain as a function of time: $\Delta\gamma_1 \sim J_1(\psi)ck_m t$. This is shown in Fig. 2(d). Not only do the higher harmonics oscillate in time, their energy contribution is small due to the coefficient $J_n(\psi)$. Because acceleration will occur over distances much longer than the modulation period, we can neglect the contribution from the non-phase-matched harmonics. The expression for the time-dependent energy gain is then

$$\Delta\gamma \simeq 2\delta a_0\left[1+\frac{2\lambda_p^2}{\pi^2 w_{ch}^2}\right]^{-1}\left(\frac{ct}{w_{ch}}\right), \tag{10}$$

where $\lambda_p=2\pi c/\omega_{p,0}$.

As discussed in the previous section, the group velocity of the guided mode in the channel is subluminal. An electron traveling at approximately c will then outrun the pulse in the pulse length dephasing time $t\sim\sigma_z/(c-v_g)$ which places a limit on the interaction time. Upon some algebra, we then obtain an expression for the pulse length limited energy gain in quasi-phase-matched direct acceleration as follows:

$$\Delta\gamma|_{QPMA} \simeq 4\delta a_0\left(\frac{\sigma_z}{w_{ch}}\right)\left(\frac{\lambda_p}{\lambda}\right)^2\left(1+\frac{2\lambda_p^2}{\pi^2 w_{ch}^2}\right)^{-2}. \tag{11}$$

The energy gain scales linearly with both the amplitude of the density modulations δ, and the field amplitude a_0. Because thinner plasma channels can support higher axial electric fields, the energy gain is inversely proportional to w_{ch}. The interaction length can be extended by increasing the pulse length σ_z, or by increasing the group velocity, which is represented by the factor $(\lambda_p/\lambda)^2(1+2\lambda_p^2/\pi^2 w_{ch}^2)^{-2}$ in Eq. (11).

Equation (11) can be compared to similar equations predicting the energy gain in other acceleration schemes. For comparison, we consider parameters similar to those used in Ref. [21]: a laser wavelength $\lambda=800$ nm, a matched beam width of $w=15$ μm, a normalized amplitude $a_0=0.25$ (corresponding to a laser power of 2 TW), a pulse duration $\sigma_t=300$ fs, an on-axis plasma density $n_0=7\times10^{18}$ cm^{-3}, a corrugation amplitude $\delta=0.9$, and a modulation period of $T_m=0.035$ cm (these parameters will be used throughout the rest of the paper unless otherwise stated). A slightly larger density amplitude modulation is used, which may be obtainable upon further experimental exploration. With these parameters, the predicted energy gain for direct acceleration in the corrugated plasma waveguide is $\Delta\gamma|_{QPMA}\sim1000$.

By comparison, the dephasing-limited energy gain for resonant laser-wakefield acceleration is [24]

$$\Delta\gamma|_{LWFA}\simeq\frac{a_0^2}{(1+a_0^2/2)^{1/2}}\left(\frac{\lambda_p}{\lambda}\right)^2\left(1+\frac{\lambda_p^2}{\pi^2w_{ch}^2}\right)^{-1}. \quad (12)$$

For the parameters listed, $\Delta\gamma|_{LWFA}\sim14$. As expected, direct acceleration produces higher gradients at lower laser powers. In the best case scenario, for semi-infinite vacuum acceleration the energy gain is given by $\Delta\gamma|_{SIVA}\simeq a_0\gamma_0/2$ [15], where γ_0 is the initial electron energy; this only provides an energy gain of $\Delta\gamma|_{SIVA}\sim13$. The energy scaling for vacuum beat wave acceleration is given as [16]

$$\gamma_f^2=\gamma_0^2+8\pi^2\left(\frac{a_0w_{ch}}{\lambda_1}\right)^2\left(\frac{\lambda_1}{\lambda_2}-1\right). \quad (13)$$

For $\lambda_1=2\lambda_2$ the predicted energy gain is $\Delta\gamma|_{VBWA}\sim9$. For parameters achievable on an actual tabletop laser at low power, the scaling laws predict that the energy gain in quasi-phase-matched acceleration exceed those of other schemes by at least an order of magnitude. The derived scaling law for quasi-phase-matched acceleration will be validated in the next section.

IV. BEAM DYNAMICS

To study electron beam dynamics and validate the energy scaling, we integrate the fully relativistic electron equations of motion in the laser electromagnetic field determined by Eqs. (2) and (3), and the condition that $\vec{\nabla}\cdot\vec{A}=0$, while neglecting space-charge effects. After the electromagnetic forces have been found, we provide estimates on the maximum beam density for which neglecting the space charge is valid.

A. Equations of motion

We write the generalized electron equation of motion as

$$\frac{d\vec{p}}{dt}=-\frac{q}{c}\left(\frac{\partial\vec{A}}{\partial t}-\vec{v}\times\vec{\nabla}\times\vec{A}\right), \quad (14)$$

where $\vec{p}=\gamma m_e\vec{v}$ and $\gamma^2=1+|\vec{p}/m_ec|^2$. Recalling that $\lambda/w_{ch},\omega_p/\omega,\lambda/\lambda_m\ll1$, we can write the three simplified components of Eq. (14) in terms of $A_\perp$ as follows:

$$\frac{dp_r}{dt}=\frac{L^2}{m_er^3}+q\kappa\left[1-\frac{v_z}{c}\left(1+\kappa^{-2}\frac{\partial}{\partial r}\vec{\nabla}\cdot\hat{r}\right)\right]A_\perp, \quad (15)$$

$$L=\text{const}, \quad (16)$$

$$\frac{dp_z}{dt}=-q\left[(\vec{\nabla}\cdot\hat{r})-\kappa\frac{v_r}{c}\left(1+\kappa^{-2}\frac{\partial}{\partial r}\vec{\nabla}\cdot\hat{r}\right)\right]A_\perp, \quad (17)$$

where $L=\gamma m_er^2\dot{\theta}$, $\kappa(z,t)=ik_0-2(z-ct)/\sigma_z^2$, and taking twice the real part, $2\,\mathrm{Re}[\ ]$, is understood, but not symbolically written. The first bracketed term in Eq. (15) is the force due to the transverse electric field. The last two terms, proportional to v_z, are the contribution from the magnetic field (the $\vec{v}\times\vec{B}$ force). The last term, in particular, is a contribution due to the finite spot size of the laser, which will have important consequences on the transverse dynamics. The constancy of $L=\gamma m_er^2\dot{\theta}$ is a result of using the azimuthally symmetric, lowest transverse magnetic mode of the channel. The first force in the z direction is simply the z component of the laser electric field which will accelerate the electron to high energies. The second force, which is smaller by $\sim(w_{ch}/\lambda)\times(v_\perp/c)$, is the contribution to the longitudinal Lorentz force from the magnetic field. For this paper, we consider electron beams with zero initial beam divergence, $\vec{J}_b(r,z,t=0)=J_b(r,z,t=0)\hat{z}$, where J_b is the electron beam current density. In this case, the force from the second term in Eq. (17) is small over the entire interaction length, and the z component of the laser electric field provides the dominant force. We do, however, keep this term in our simulation, but neglect it in our analysis of the beam dynamics later on. Equations (15)–(17) are integrated over the waveguide-limited interaction time, which is the time it takes an electron going nearly c to travel the length of the waveguide. For our simulations the waveguide length is set to 1.8 cm corresponding to waveguides created in Ref. [21]. It should be noted that for our case, the waveguide-limited interaction time is less than the pulse length dephasing time by a factor of ~2; the maximum energy gain will thus be limited by the waveguide length.

B. Scaling law validation

To validate the scaling law, the electron trajectories were initiated on axis from -10 μm to -11 μm behind the peak of pulse (one micron is approximately a wavelength or a percent of the full width half maximum). The initial transverse momentum of the electrons was set to zero, and the initial axial momentum p_z/m_ec was set to three different values: 30, 100, and 1000. Figure 3 shows a comparison of our scaling law from Eq. (11) with simulated electron trajectories that have been phase selected to produce the highest energy gain over the waveguide-limited interaction length. In Fig. 3(a), the effective phase velocity of the $n=1$ spatial harmonic is matched to three different initial electron velocities by tuning the modulation period, which could be accomplished experimentally by inserting imaging optics in the radially modulated channel formation beam shown in Fig. 1. For an initial energy of $\gamma_0=30$ the electron begins to accelerate but

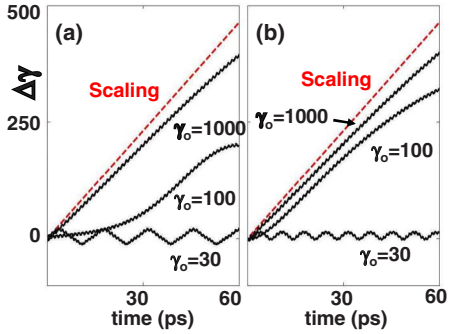

FIG. 3. (Color online) Comparison of energy gain predicted by our scaling law, dotted (red) with numerical results obtained by integrating the fully relativistic electron equations of motion. (a) The slow wave phase velocity is matched to the initial electron velocity. (b) The slow wave velocity is set to c.

quickly becomes dephased from the $n=1$ spatial harmonic as its velocity increases. The electron is then decelerated and again becomes phase matched. For $\gamma_0=100$ the electron and slow wave remain phase matched longer; the increase in electron energy results in a small change to its velocity. The electron does begin to outrun the slow wave towards the end of the waveguide. As expected, we see the best agreement with the scaling law for an initial energy of $\gamma_0=1000$. The electron's velocity remains essentially constant, and phase matching is maintained over the entire waveguide.

In Fig. 3(b) the phase velocity of the $n=1$ spatial harmonic was set to c for all three initial electron energies. The $\gamma_0=30$ trajectory never catches up with the spatial harmonic and experiences alternating regions of acceleration and deceleration as the slow wave continually sweeps past it. The $\gamma_0=100$ electron gains more energy than when it started phase matched with the spatial harmonic. Before the electron begins to dephase, it is accelerated up to the slow wave phase velocity. The electron spends more time in the acceleration phase and as a result gains more energy. For $\gamma_0=1000$ the change is minimal; the phase velocity for the $n=1$ spatial harmonic in the previous case was essentially c already.

The limitations of our scaling law are apparent in Figs. 3(a) and 3(b). The scaling law assumed phase matching over the entire interaction length, and cannot be applied to lower energies for the distances considered here, explaining the large discrepancy for $\gamma_0=30$ and $\gamma_0=100$. As stated previously, for low initial energies gradients in the modulation period or background density are required to maintain phase matching over longer distances. Furthermore, our scaling law assumes a constant pulse amplitude over the entire pulse length (a flat top pulse), whereas the pulse in the simulation was Gaussian. The discrepancy in the slope of the scaling law and the energy gain of the $\gamma=1000$ particle is a result of the smaller field amplitude experienced by the electron as it moves through the pulse. The resulting energy gains from the simulations for $\gamma_0=100$ are still at least an order of magnitude better than the energy gains from both laser wakefield acceleration and other direct acceleration schemes.

A simple Hamiltonian model for the longitudinal dynamics explains the features observed in Fig. 3. We start with equations describing the evolution of the energy and phase of an electron as follows:

$$\frac{d\gamma}{dz} = k_0 \hat{a}_0 \cos(\varphi), \tag{18}$$

$$\frac{d\varphi}{dz} = k - \frac{\omega_0}{v_z(\gamma)}, \tag{19}$$

where $\varphi=kz-\omega_0 t$, $k=k_0+\delta k+k_m$, $\hat{a}_0=4J_1(\psi)a_0/k_0 w_{ch}$, and it has been assumed that the electron starts on axis near the peak of the pulse. From Eqs. (18) and (19) we find that the Hamiltonian is given by

$$H = k\gamma - k_0(\hat{a}_0 \sin(\varphi) + \sqrt{\gamma^2 - 1}). \tag{20}$$

We note that $k_0/k=v_{p,1}/c$, where $v_{p,1}$ is the phase velocity of the $n=1$ spatial harmonic. H contains no explicit dependence on z and thus $dH/dz=0$ or $H(\gamma_0,\varphi_0)=H(\gamma,\varphi)$, where γ_0 and φ_0 are the initial relativistic factor and phase of the electron, respectively.

For mathematical simplicity, we first consider the case when $k_0/k=1$ or $v_{p,1}=c$, corresponding to Fig. 3(b). The electron velocity is then less than the $n=1$ phase velocity. Equation (20) then has one solution for $\gamma(\varphi)$ as follow:

$$\gamma(\varphi) = \frac{1 + [k_0^{-1}H + \hat{a}_0 \sin(\varphi)]^2}{2[k_0^{-1}H + \hat{a}_0 \sin(\varphi)]}. \tag{21}$$

Setting $d\gamma/d\varphi_0=0$ and solving for φ_0, we determine what initial phase results in the maximum energy gain: $\varphi_{0,\max}=\pi/2$. As expected, the maximum energy occurs when the electron starts at a zero of the accelerating field and experiences the entire accelerating phase as the slow wave passes by. We will consider the motion of the maximum accelerated electron and thus set $H=H(\gamma_0,\pi/2)$.

The denominator of Eq. (21) shows that there is a critical initial energy, $\gamma_{0,crit}=(1+4\hat{a}_0)/4\hat{a}_0$, which we rewrite for our parameters using the fact that $\hat{a}_0 \ll 1$,

$$\gamma_{0,crit} \simeq \left(\frac{k_m w_{ch}}{4\delta a_0}\right)\left(\frac{\omega}{\omega_{p,0}}\right)^2. \tag{22}$$

Above $\gamma_{0,crit}$, the electron will continually gain energy as it phase slips with respect to the field. Furthermore, for energies above $\gamma_{0,crit}$, the electron phase slippage is limited; the electron can phase slip by at most $\varphi_{\max}=\sin^{-1}[H(\gamma_0,\varphi_0)/k_0\hat{a}_0]$. For energies below $\gamma_{0,crit}$, electrons can phase slip by 2π radians and, as a result, undergo energy oscillations as the slow wave fronts continually move past them. The maximum energy for $\gamma_0<\gamma_{0,crit}$ is $\gamma(-\pi/2)$. For our parameters $\gamma_{0,crit}\simeq 81$; both the $\gamma_0=100$ and $\gamma_0=1000$ cases are above $\gamma_{0,crit}$, explaining their steady increase in energy. $\gamma_0=30$ is below $\gamma_{0,crit}$ which explains the energy oscillations. Equation (22) also shows that the critical energy can be reduced by increasing the modulation period; for accelerating low energy electrons, longer modulation periods are preferable.

We now consider the case where the initial electron velocity is matched to the $n=1$ phase velocity, $v_{p,1}=v_{z,0}$. The Hamiltonian constant is given by $H(\gamma_0,\varphi_0)=k/\gamma_0-k_0\hat{a}_0$, and

because we are interested in relativistic electrons $k_0/k \simeq 1 - 1/2\gamma_0^2$. Solving Eq. (20) for γ, we have for large electron energies, $\hat{a}_0\gamma_0/2 \gg 1$, that

$$\frac{\gamma(\varphi)}{\gamma_0} \simeq 1 + 2\gamma_0\hat{a}_0[1 - \sin(\varphi)], \tag{23}$$

where the maximum energy gain is given by $\Delta\gamma_{\max} = (\gamma_0/\gamma_{0,crit})\gamma_0$. The large energy limit corresponds to our $\gamma_0 = 1000$ case in Fig. 3(a). When the electron velocity and $n=1$ phase velocity are initially matched there is a limit on the maximum energy gain due to the electron outrunning the slow wave. Our parameters give $\Delta\gamma_{\max} \simeq 1.2 \times 10^4$, which explains the similarity between Figs. 3(a) and 3(b); the $\gamma_0 = 1000$ electron had not yet approached its maximum energy. For lower electron energies $\hat{a}\gamma_0/2 \ll 1$, we have that

$$\frac{\gamma(\varphi)}{\gamma_0} \simeq 1 + \sqrt{2\gamma_0\hat{a}[1 - \sin(\varphi)]} + \gamma_0\hat{a}[1 - \sin(\varphi)], \tag{24}$$

where the maximum energy gain is given by $\Delta\gamma_{\max} = [(\gamma_0/\gamma_{0,crit})^{1/2} + (\gamma_0/2\gamma_{0,crit})]\gamma_0$, and we have retained an extra order in $(\gamma_0/\gamma_{crit})^{1/2}$ to better match our results. When $\gamma_0 = 100$, we find that $\Delta\gamma_{\max} \simeq 210$ similar to the value found in Fig. 3(a). The energy gain for the $\gamma_0 = 100$ electron is limited when $v_{p,1} = v_{z,0}$, explaining the higher yields in Fig. 3(b).

Figures 3(a) and 3(b) also show a rapid oscillation due to the longitudinal force of the fundamental $n=0$ laser mode, with the oscillation frequency determined by the difference between the laser fundamental phase velocity and the electron phase velocity, cL_d. Although not visible, the electron also undergoes rapid oscillations due to all other spatial harmonics at a frequency $(n-1)ck_m$, but the amplitude of these oscillations becomes diminishingly small as n is increased $\sim \psi^n/2^n n(n!)$. The rapid oscillations due to $n=0$ will become important when considering the transverse electron motion.

C. Transverse dynamics

For examining the transverse dynamics of the electron beam, electrons were distributed uniformly in the axial direction from -1 μm to -11 μm behind the peak of the pulse and as a Gaussian in the radial direction with varying width σ_b. The initial electron momentum was set to $p_z/m_e c = 100$ and the phase velocity of the $n=1$ spatial harmonic was set to c.

Figure 4 shows the final electron distribution functions as a function of momentum on a log scale after 60 ps, the waveguide limited interaction time. When all the electrons start on axis ($\sigma_b = 0$), the distribution function contains a quasimonoenergetic peak at $p_z/m_e c \simeq 400$ with a full width at half maximum value of 8 MeV (a relative width of $\sim 4\%$). The distribution function is also asymmetric about the initial momentum. For larger initial energies, we would expect a distribution function symmetric about the initial momentum; dephasing over the interaction length would be negligible, and an equal number of electrons would start in the accelerating phase as in the decelerating phase. Here some electrons have the proper z_0 (initial phase) to be accelerated up to the slow wave, which, as discussed above, can result in higher energies. The remaining electrons are initially accelerated or decelerated based on their phase. These electrons are never properly phase matched and their phase slippage results in a slow spreading of the distribution function about the initial momentum.

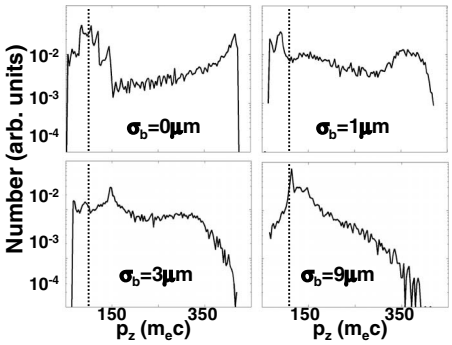

FIG. 4. Electron axial momentum distributions for different initial electron beam widths after 1.8 cm of propagation (the extent of a physical plasma waveguide).

As the width of the electron beam is increased from $\sigma_b = 0$ to $\sigma_b = 9$ μm the quasimonoenergetic peak is lost. The increased electron beam radius places more electrons in the low amplitude periphery of the accelerating field, which decreases as a function of radius, $A_z \propto 1 - 2r^2/w_{ch}^2$. Figure 5, which shows a comparison of the Gaussian widths of the electron beam to the axial field profile, suggests, however, that for $\sigma_b = 1$ μm and 3 μm most of the electrons still experience the peak of the accelerating field. The loss in the high energy peak is then a result of the transverse motion of the beam electrons.

Some of the features of the transverse dynamics are depicted in the multimedia file linked in Ref. [25]. The movie shows a subset of electrons distributed uniformly in z from -10 μm to -11 μm behind the peak of the laser with $\sigma_b = 6$ μm. The vertical scale is radius and the horizontal scale is $z - ct$, following the movement of the electron beam; both scales are in microns. The color scale is in units of energy normalized to rest mass and changes as the beam propagates. The electrons in the decelerating phase experience a large transverse force and are expelled from the center of the elec-

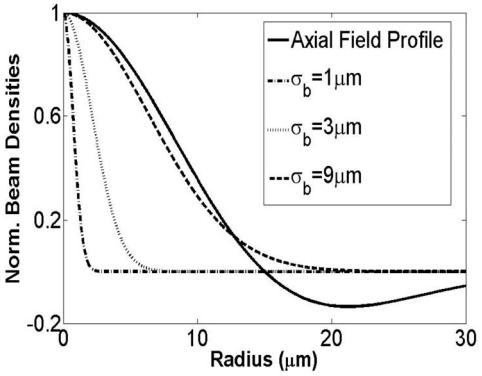

FIG. 5. Comparison of electron beam Gaussian widths with axial field profile.

tron beam. The accelerated electrons remain mostly collimated towards the center of the beam, but undergo a slow transverse spreading. The collimation of the higher energy electrons can be used for spatial filtering of the electron beam if quasimonoenergetic peaks are desired. To examine the transverse dynamics in detail, we turn to the transverse equations of motion.

An electron displaced from the axis will experience two types of transverse force in the absence of space charge. For an electron close to the axis, near the peak of the laser pulse, we can write the transverse equation of motion as

$$\frac{dp_r}{dt} = \frac{q}{c}\left[\frac{\partial}{\partial t} + v_z\frac{\partial}{\partial z} - v_z\left(\frac{2}{w_{ch}}\right)^2\frac{2}{ik_0}\right]A_\perp. \tag{25}$$

Inserting the solution for $A_\perp$, and using the phase-matching condition for the $n=1$ spatial harmonic, we obtain an expression for the quasi-phase-matched focusing or defocusing force due to the slow wave as follows:

$$F_r^{qpm} = \frac{m_e c^2 k_0 \delta a_0}{[1+2\lambda_p^2/(\pi^2 w_{ch}^2)]}\frac{r}{w_{ch}}\left[1 - \frac{v_z}{c}\left(1+\frac{8}{k_0^2 w_{ch}^2}\right)\right] \times \cos(k_0 z - \omega_0 t). \tag{26}$$

This is the transverse force associated with the phase-matched axial accelerating force. The axial and transverse forces are 90° out of phase. As observed in the multimedia file, electrons in the maximum axial accelerating phase experience no quasi-phase-matched focusing or defocusing. The force is either focusing or defocusing depending on the phase of the electron z. In particular, for an axial uniform distribution of highly relativistic electrons for which $\varphi = k_0 z - \omega_0 t$ is constant over the entire interaction length an equal number of electrons experience focusing as defocusing. From Eq. (26) we can estimate the shortest time scale for the growth of the focusing or defocusing for orbits slightly off axis as

$$\tau \sim \left(\frac{2\pi}{\omega_0}\right)\left(\frac{c}{c-v_z}\right)^{5/6}\left[\frac{(k_0 w_{ch})(k_0\lambda_p)(k_m\lambda_p)}{16\sqrt{2}\pi^5\delta a_0}\right]^{1/3}. \tag{27}$$

For our parameters we find that $\tau \sim 12$ ps for $\gamma_0 = 100$, consistent with simulated electron trajectories shown in the Ref. [25].

The terms proportional to v_z in Eq. (26) result from the $\vec{v}\times\vec{B}$ contribution to the Lorentz force. For plane waves as the axial velocity approaches c the quasi-phase-matched transverse force becomes diminishingly small. Because the pulse has a finite spot size, we obtain a correction $8/k_0^2 w_{ch}^2$, that reduces the velocity where the transverse force vanishes. Specifically, we find that the transverse force vanishes when $\gamma = k_0 w_{ch}/2\sqrt{2}$, which for our parameters is $\gamma_0 \simeq 42$. By matching the injection energy to $k_0 w_{ch}/2\sqrt{2}$, deflection of the electron beam can be limited in the early stages of acceleration. Furthermore, this suggests that by adiabatically changing the channel radius over the interaction length, $w_{ch}(z) = 2\sqrt{2}\gamma(z)/k_0$, it may be possible to maintain a collimated beam, which will be a topic of future research.

The forces due to the other spatial harmonics ($n \neq 1$) also contribute to the transverse motion of the electron beam. As discussed earlier, the electron moves through the phase fronts of these harmonics and undergoes rapid oscillatory motion, $\omega_{osc} \sim (n-1)ck_m$. Over the entire interaction length the oscillations undergo many cycles, $k_0\sigma_z$ (for our parameters $k_0\sigma_z \sim 700$). The oscillations themselves thus contribute little to the long term directed motion of the electron beam. However, because of the spatial variation of the field envelope the oscillations can beat and give rise to directed motion through their ponderomotive force on the electron beam. The $n=0$ spatial harmonic provides the dominant contribution to this motion on account of its large relative amplitude.

Expanding around the initial electron velocity $\vec{v} = v_0\hat{z}$ and averaging over the fast time scale $k_m v_z$, we have to lowest order in λ/w_{ch},

$$F_r^{pm} = -\frac{1}{2m_e\gamma_0}\nabla\langle p_{1,r}^2\rangle, \tag{28}$$

where the angled brackets denote the time averaging. The contribution to the ponderomotive force from the first order axial momentum $p_{1,z}$, which accounts for corrections to the initial momentum $p_{0,z} = m\gamma_0 v_0$, provides corrections to Eq. (28) of order $(\lambda/w_{ch})^2$ and has been neglected. Inserting our expression for the axial field, we obtain the ponderomotive force due to the fundamental $n=0$ laser mode for small radii near the peak of the laser pulse as follows:

$$F_r^{pm} = -\frac{2m_e c^2}{\gamma_0}\frac{r}{w_{ch}^2}a_0^2\left[1 - \frac{4}{\pi^2}\frac{v_0}{c}\left(\frac{\lambda_p}{w_{ch}}\right)^2\left(1+\frac{2\lambda_p^2}{\pi^2 w_{ch}^2}\right)^{-1}\right]^2. \tag{29}$$

The force is independent of the electron's phase. In addition, the hollow profile of the transverse field results in an inward force. The ponderomotive force thus provides a focusing over the entire electron beam. Higher energy electrons will experience a smaller ponderomotive focusing due to the inverse dependence on γ_0, further explaining the small transverse excursions observed in the multimedia file [25]. The second term in the brackets, which results from the finite spot-size, reduces the focusing effect of the ponderomotive force. The finite spot-size correction is not necessarily negligible, and for our case is ~ 0.25.

The ponderomotive force when taken in addition to the quasi-phase-matched focusing or defocusing force provides an overall focusing of the electron beam for small radii. The overall focusing is limited by the amplitude of the ponderomotive force, which is typically smaller than the quasi-phase-matched focusing or defocusing force except near the maximum accelerating phase. The phase independent ratio of the forces is

$$F_r^{pm}/F_r^{qpm} \sim \frac{1}{4\gamma_0}a_0\left(\frac{k_0 w_{ch}}{\delta}\right)\left(1+\frac{\lambda_p^2}{\pi^2 w_{ch}^2}\right)^{-1}, \tag{30}$$

which for our parameters $F_r^{pm}/F_r^{sw} \sim 0.08$.

Figures 6 and 7 show the number-averaged final z momentum in units of $m_e c$ as a function of initial and final position, respectively, for an initial electron beam radius of $\sigma_b = 9$ μm. The accelerated electrons started in buckets one half of a slow wavelength long. Buckets are limited in the

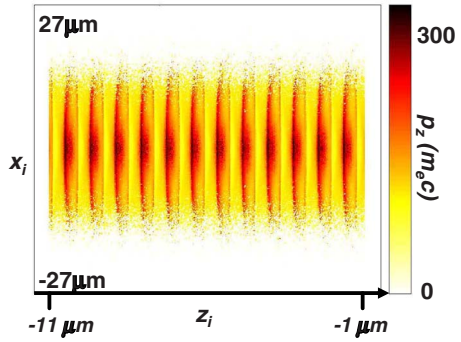

FIG. 6. (Color online) Averaged final (after 1.8 cm of propagation) axial momentum as a function of initial position (x_i, z_i).

transverse direction by the laser spot size. After acceleration the momentum is concentrated in z as the high energy electrons move towards the front of the slow wave, but is spread transversely as some of the electrons in the accelerating phase are initially defocused. Figure 8 shows the final electron beam density as a function of position; the beam has acquired a significant transverse spread which peaks off axis. Comparing Figs. 7 and 8 we see that these peaks are mostly composed of lower energy electrons that have been expelled from the center of the electron beam. As seen in the multimedia file and predicted by our analysis the high energy electrons remain collimated at the center of the beam. They see little to no focusing or defocusing quasimatched force, and only the small focusing ponderomotive force.

The electron beam experiences a net outward density flow as seen in Fig. 8. At radii greater than $w_{ch}/\sqrt{2}$, electrons that were initially defocused move outside the peak of the hollow mode fields and experience a larger defocusing force due to the ponderomotive force switching sign. These electrons are expelled from the beam. Eventually electrons initially in a focusing phase begin to phase slip and enter the defocusing phase where they undergo the same process.

Many of the transverse effects on the electron beam can be managed by increasing the radius of the plasma channel (matched laser spot size). Increasing the spot size increases the defocusing time in Eq. (27) as $\tau \sim w_{ch}^{1/3}$. Furthermore, for highly relativistic injection energies the quasi-phase-matched

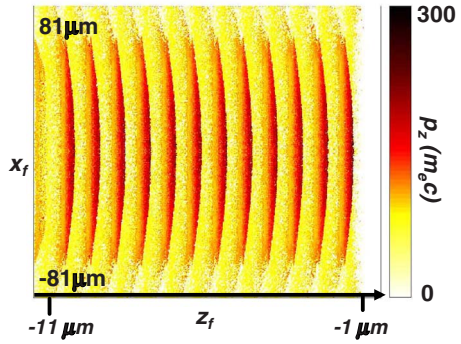

FIG. 7. (Color online) Averaged final (after 1.8 cm of propagation) axial momentum as a function of final position (z_f, x_f) (the axial distance traveled by the leading electron has been subtracted out).

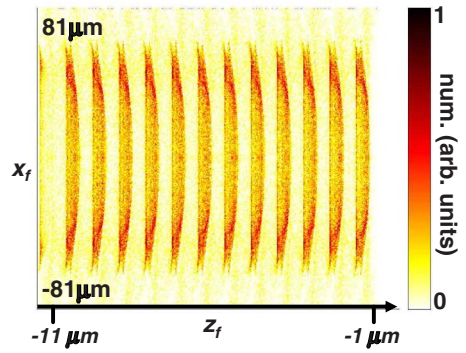

FIG. 8. (Color online) Final electron density as a function of final position (z_f, x_f). The electrons are accelerated into the slow wave fronts resulting in bunching.

defocusing can be reduced by decreasing the finite spot-size correction to the Lorentz force. At the same time, the ponderomotive focusing force would be increased due to the reduction in the spot-size correction. The outward flow of beam electrons can also be minimized by using electron beams with widths less than $w_{ch}/\sqrt{2}$ (for our case $\sqrt{2}\sigma_r/w_{ch} \sim 0.85$). Due to limitations on injection beams, it may be easier to increase the channel radius than decrease the electron beam radius. Unfortunately, by increasing the channel radius the predicted energy gain of the electrons decreases, $\Delta\gamma \sim w_{ch}^{-1}$. This can be overcome by maintaining the ratio of the field amplitude to the spot size, a_0/w_{ch}=const. This, however, greatly increases the laser power requirements for quasi-phase-matched direct acceleration, $P \sim (a_0 w_{ch})^2 \sim w_{ch}^4$. In instances where power is not a limiting factor, larger spot sizes can greatly improve the quality of the accelerated electron beam.

D. Space-charge estimation

For a simple estimate of the magnitude of the transverse space-charge force we consider a uniform cylindrical electron beam. We suppose the electron beam is infinitely long so that we may ignore longitudinal edge effects and thus ignore any axial electric field due to the beam. Noting that the electrons themselves give rise to a radial electric field and that their motion gives rise to an azimuthal magnetic field, we find the space-charge force to be

$$F_r^{sc} = \frac{1}{2} m_e \omega_{p,b}^2 \left(1 - \frac{v_z^2}{c^2}\right) r, \tag{31}$$

where $\omega_{p,b}$ is the plasma density of the electron beam. The first term in parentheses is the result of the beam's electric field, and the second term is due to the beam's magnetic field. We note that for highly relativistic beams the transverse space-charge force can be neglected altogether.

The maximum allowable charge density can be estimated by forming the ratio of the transverse space-charge force to the quasi-phase-matched focusing or defocusing force, F_r^{sc}/F_r^{qpm} as follows:

$$n_{e,b}[\mathrm{cm}^{-3}] < \frac{2.3\times 10^{12}}{(1+2\lambda_p^2/\pi^2 w_{ch}^2)}\left(\frac{\delta a_0}{k_0 w_{ch}}\right)\frac{w_{ch}^{-2}[\mathrm{cm}^{-2}]}{(1-v_z/c)}, \quad (32)$$

where $n_{e,b}$ is the electron beam density, and we have assumed $v_z \simeq c$. Equation (32) uses the maximum focusing phase of the quasi-phase-matched force and as a result is phase independent; the actual maximum charge will be lower by approximately one order of magnitude. For our parameters with v_z corresponding to $\gamma_0=100$ and including an order of magnitude for phases where the transverse force may be smaller, we find that $n_{e,b}<3\times 10^{18}$ cm^{-3}. For a uniform cylindrical beam with a length and radius of 10 μm, $n_{e,b}=3\times 10^{18}$ cm^{-3} corresponds to 10^{10} electrons.

To estimate the longitudinal space-charge force, we consider the electron beam after acceleration when the electrons have accumulated at the slow wave fronts as shown in Fig. 8. If the electron bunch spacing is much smaller than the beam length, the force on one bunch due to adjacent bunches can be neglected. The local Poisson equation for an electron bunch is then

$$\vec{\nabla}\cdot\vec{E} = 4\pi q n_{e,b}\left(\frac{\lambda_b}{2\pi}\right)\delta(z), \quad (33)$$

where $\lambda_b=2\pi/(k_0+\delta k+k_m)$ is the spacing between bunches. Integrating over the axial coordinate we obtain the local longitudinal space-charge force

$$F_z^{sc} = 2q\lambda_b n_{e,b}. \quad (34)$$

Forming the ratio F_z^{sc}/F_z^{qpm}, we find an expression for the maximum allowable beam density.

$$n_b[\mathrm{cm}^{-3}] < \frac{3.6\times 10^{12}}{[1+\lambda_p^2/\pi^2 w_{ch}^2]}\delta a_0 (w_{ch}\lambda_0)^{-1}[\mathrm{cm}^{-2}]. \quad (35)$$

For the parameters used in our simulations we find that $n_{e,b}<6.3\times 10^{18}$ cm^{-3} similar to the value obtained for the transverse space-charge force. Unlike the longitudinal space-charge force, the expression is naturally phase independent due to the axial bunching of the electrons. Also, the allowable density does not increase as the electron's axial momentum increases; for highly relativistic electron beams the actual bound on the density is provided by the expression for the longitudinal space-charge force, Eq. (35).

V. SUMMARY AND CONCLUSIONS

We have developed an analytic model for laser pulse propagation in a corrugated plasma waveguide, using the slowly varying envelope approximation. The background plasma was assumed to be a cold nonrelativistic fluid that responded linearly to the laser field. The plasma density profile was chosen to model the density profiles created in experiments [21], while at the same time providing an analytic solution, facilitating analysis of the electron beam dynamics. The field structure of the laser was examined. It was shown that as a result of the axial periodic density profile, the guided mode is composed of spatial harmonics. For a small enough plasma corrugation period the phase velocity of the spatial harmonics could be subluminal—a requirement for electron acceleration. The contribution of each spatial harmonic was determined by its relative amplitude, which, for parameters of interest, was shown to decrease significantly with an increasing harmonic number. Only the first few spatial harmonics contributed to the field structure in the plasma channel. The spatial harmonics can also be viewed as a periodic phase modulation of the guided mode. The spatially local phase velocity of the guided mode was shown to oscillate at the modulation period.

With the solution for the electromagnetic field, a scaling law for the energy gain via quasi-phase-matched direct acceleration was derived. The term quasiphase matched refers to matching the electron velocity to the phase velocity of a spatial harmonic. The fundamental laser mode is strictly superluminal, thus quasiphase matching requires the presence of subluminal spatial harmonics. Due to the drop-off in amplitude of spatial harmonics with an increasing harmonic number, the first spatial harmonic was chosen as the phase-matched mode. The scaling law compared favorably to both laser wakefield acceleration and other direct laser acceleration schemes, predicting energy gains in excess of an order of magnitude higher for actual tabletop laser parameters.

To validate the scaling law and examine the transverse dynamics, simulations of electron trajectories in the presence of the laser's electromagnetic field were conducted. Space-charge forces were ignored, and estimates of the validity of this omission were later provided in terms of allowable electron beam densities. Scaling law validations showed close agreement for an initial electron energy of $\gamma_0=1000$. A discrepancy in the slope of the energy gain as a function of time was a result of using a Gaussian pulse in the simulations and a flattop pulse when calculating the scaling law. For initial energies of $\gamma_0=100$, it was shown that allowing the electron to catch up to the spatial harmonic phase velocity yielded higher energy gains than starting the two perfectly phase matched; the electron acceleration resulted in phase slippage with respect to the spatial harmonic. For lower energies $\gamma_0=30$, phase slippage occurs rapidly, and graded modulation periods or tapered axial densities are required for acceleration over waveguide limited distances. These results were explained using a simple Hamiltonian model for the longitudinal dynamics.

Two forces were responsible for the transverse dynamics of the electron beam: the quasi-phase-matched focusing or defocusing force, and the ponderomotive force due to the fundamental laser mode. The quasi-phase-matched force focuses or defocuses based on the electron's phase, whereas the ponderomotive force focuses regardless of phase for small radii. Both forces contained a correction due to the finite spot size of the laser. The quasi-phase-matched transverse force is 90° out of phase with the quasi-phase-matched axial force; electrons in the maximum accelerating phase only experience a ponderomotive transverse force. As a result, highly accelerated electrons remain collimated in the electron beam, while the remaining electrons are expelled from the beam. A net outward flow of electrons resulted from initially focused electrons slipping into the defocusing phase, and the ponderomotive force causing defocusing at large radii.

ACKNOWLEDGMENTS

The authors would like to acknowledge support from the DOE and NSF.

APPENDIX A: NONLINEAR AND RELATIVISTIC PLASMA EFFECTS

The assumption of linear plasma response is not always valid in the regime of high intensity lasers where the effect of the ponderomotive force on the background plasma becomes important. We seek to find an estimate of the relative density fluctuations due to the ponderomotive force and show that for the laser intensities considered these fluctuations are small. We start with the equation for the first order motion of the density in the presence of the laser field as follows:

$$\frac{\partial^2 n_1}{\partial t^2} + \omega_{p,0}^2 n_1 = \frac{1}{4} n_0 c^2 \nabla^2 \langle \hat{a}_r^2 \rangle, \tag{A1}$$

where $\omega_{p,0}$ is the plasma frequency for the background density, the brackets represent an average over the laser frequency, $\hat{a}_r = e\hat{A}_r / m_e c^2$, and only the largest amplitude fundamental laser harmonic is considered. By replacing the Laplacian with its peak value $4a_0^2/w_{ch}^2$, which occurs at $r=0$, we obtain an estimate on the magnitude of the density perturbation due to the transverse ponderomotive force as follows:

$$\frac{n_1}{n_0} \sim \frac{1}{4\pi^2} a_0^2 \left(\frac{\lambda_p}{w_{ch}} \right)^2, \tag{A2}$$

which for the parameters considered here gives $n_1/n_0 \sim 0.001$. This ratio seems to justify ignoring the ponderomotive current in Eq. (2). It should be noted that $\partial^2 \langle \hat{a}_r^2 \rangle / \partial z^2 = 0$ at $r=0$, the peak of the Laplacian. However, the density perturbation is excited by the maximum of ∇^2, wherever it occurs. In addition, the pulse length considered is much longer than the spot size, making the longitudinal contribution to the displaced charge negligible.

By including a correction to Eq. (2) corresponding to a ponderomotive driven modulation of the electron density, but maintaining the slowly varying envelope approximation, we can describe Raman side scattering (RSS) of the laser pulse. RSS can cause rapidly growing perturbations in the plasma density and pulse profile which can severely limit the accelerating gradient of the laser electric field. Antonsen and Mora have suggested, however, that the unstable growth due to RSS can be suppressed by utilizing leaky density profiles, allowing for the stable propagation of the lowest radial eigenmode of the plasma channel [26]. The remaining eigenmodes are not confined to the channel and are damped, preventing their growth.

In order to neglect the generation of higher order eigenmodes, we must stipulate that our density profile given in Eq. (3) is meant to model a leaky channel with one well confined quasibound mode. In addition, the actual mode profile for the leaky channel must be accurately represented by our solution to Eq. (2). From WKB theory we obtain the condition for modes as follows:

$$\int_{r_{i,\ell}}^{r_{0,\ell}} k_{\perp,\ell} dr = \frac{\pi}{2} \left(\ell + \frac{1}{2} \right), \tag{A3}$$

where $ck_{\perp,\ell} = [2c^2 k_0 |\delta k_\ell| - \langle \omega_p^2(r) \rangle_z - 3c^2/4r^2]^{1/2}$, which has roots at the inner and outer classical turning points $r_{i,\ell}$ and $r_{0,\ell}$, respectively. We note that for different values of ℓ there are different $k_\perp$'s and different turning points. The r^{-2} term in Eq. (2) provides an effective potential that appears in our expression for $k_\perp$ and provides an inner turning point. For one quasibound mode we need to ensure that Eq. (A3) is only satisfied for $\ell = 0$ by setting the radius where the density profile is a maximum. For our model density profile, we find that

$$\delta k_\ell = -k_0 \left[\frac{\omega_{p,0}^2}{2\omega^2} + \frac{4\ell + 2 + \sqrt{3}}{k_0^2 w_{ch}^2} \right], \tag{A4}$$

and

$$r_{0,\ell}^2 = \frac{1}{2} w_{ch}^2 \left[\left(2\ell + 1 + \frac{\sqrt{3}}{2} \right) + \sqrt{\left(2\ell + 1 + \frac{\sqrt{3}}{2} \right)^2 - \frac{3}{4}} \right]. \tag{A5}$$

The outer turning point is a monotonically increasing function of ℓ. We can then ensure one quasibound mode by choosing the density to be a maximum between $r_{0,0}$ and $r_{0,1}$.

As pointed out in Ref. [26], extending the maximum density past the outer turning point $r_{0,0}$, allows for a more confined mode due to $k_\perp$ becoming evanescent. Furthermore, it allows for consistency with our lossless model density profile and boundary condition $\hat{A}_r(r \to \infty, z, t) = 0$, via the condition

$$\mathrm{Im} \left[\int_{r_{0,0}+\eta}^{\infty} k_\perp dr \right] \gg 1, \tag{A6}$$

where the density profile peaks at $r_{0,0} + \eta < r_{0,1}$. If $\eta = 0$ the integral in Eq. (A6) would be strictly real, allowing for outgoing waves, and our model boundary condition would no longer be adequate. Thus our analytic model provides a good representation of a radial density profile of the form

$$n_e(r) = \begin{cases} n_0 + n_0'' r^2/2 & 0 < r \leq r_{0,0} + \eta \\ n_1(r) & r_{0,0} + \eta < r < \infty, \end{cases} \tag{A7}$$

where $n_1(r)$ should satisfy Eq. (A6) and ensure that $n_e(r)$ is continuous. If we restrict ourselves to modeling radial plasma density profiles shown in Eq. (A7), our analytic model provides a good representation of laser propagation, while at the same time stabilizing the effect of RSS. Figure 10(a) shows a plasma density profile that is consistent with our requirements including only one quasibound mode; Fig. 10(b) shows the corresponding $k_\perp^2$.

In addition to RSS, we have neglected Raman forward scattering (RFS) by assuming linear nonrelativistic plasma response and dropping mixed derivates in Eq. (2). The growth rate for RFS perturbations to the laser is smaller than the growth rate for RSS by $\sim \omega_p / \omega_0$ [27]. However, over propagation distances required for desired interaction lengths in direct electron acceleration, these perturbations may be-

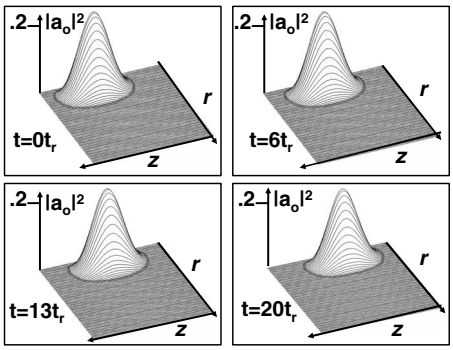

FIG. 9. The envelope of the transverse vector potential propagating in the axially modulated channel at different times in a frame moving at c. Results were obtained using the WAKE simulation [28].

come non-negligible. The pulse lengths required for extending the interaction length in direct acceleration also makes the laser more susceptible to Raman instabilities [27]. To test the effect of RFS on the pulse we conducted simulations of radially polarized laser propagation in a corrugated plasma channel with WAKE [28] for our parameters of interest. Figure 9 shows the envelope of the transverse vector potential for the radially polarized laser pulse at different Rayleigh times, where a Rayleigh time is defined as $t_R=\pi w_{ch}^2/\lambda c$ (the waveguide limited time is $20t_R$). The results show stable propagation over 20 Rayleigh lengths with no fragmentation or distortion of the laser pulse. The stable propagation is consistent with our estimate on the density fluctuations due to the presence of the ponderomotive force. Propagation was also tested in an uncorrugated channel and showed similar behavior; the underlying mechanism allowing for stable propagation of the radially polarized laser is not an artifact of the corrugated channel. The wake simulations and preceding analysis indicate that our assumptions of the plasma response are valid for the parameters and propagation distances considered.

APPENDIX B: PULSE POWER LEAKAGE FROM PLASMA CHANNEL

Our choice of model density profile given by Eq. (3) continues to increase as $r\to\infty$, providing zero vector potential as $r\to\infty$. As a result, our model pulse propagates down the length of the plasma channel without any loss due to radially outgoing waves. Actual experimental plasma density profiles peak at some finite radius and decay to zero for large radii (as seen in the density contours of Fig. 1). Depending on the density profile, the loss of pulse power to outgoing waves may be significant [21], and the accelerating gradient can be reduced as the pulse propagates. Here we want to examine the loss of pulse power due to more realistic leaky plasma channels like the one shown in Fig. 10(a) and obtain a condition for which our lossless profile is valid. In the following analysis we will neglect the axial corrugations for mathematical simplicity. The modulations will result in a modulation of the power loss that will average out when integrating over the length of the waveguide.

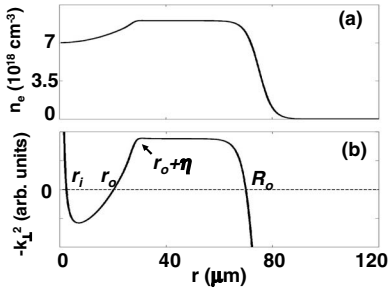

FIG. 10. A sample density profile allowing for one quasibound mode and also limiting the loss of pulse power to outgoing waves. Solutions to Eq. (2) for our model density profile in Eq. (3) accurately represent the shown density profile. (b) $k_\perp^2$ corresponding to the density profile shown in (a).

We start by writing an expression for the differential radial power flow as follows:

$$\frac{1}{r}\frac{dP}{dz}=\frac{c}{2}\mathrm{Re}[\vec{E}\times\vec{B}^*]\cdot\hat{r}, \tag{B1}$$

or equivalently

$$\frac{1}{r}\frac{dP}{dz}=\frac{c}{2}\mathrm{Re}[E_z B_\theta^*]. \tag{B2}$$

With an expression for $\hat{A}_r$, and thus A_z using $\vec{\nabla}\cdot\vec{A}\simeq 0$, we can find E_z from $\vec{E}=-\partial\vec{A}/\partial ct$, and B_θ from Faraday's law. We proceed by using the WKB approximation for finding an expression for $\hat{A}_r$ outside of the channel. As stated in Appendix A, $ck_{\perp,0}=[2c^2k_0|\delta k_0|-\langle\omega_p^2(r)\rangle_z-3c^2/4r^2]^{1/2}$, where δk_0 is given by Eq. (A4) with $\ell=0$. Figure 10(b) shows $k_{\perp,0}^2$ for a typical leaky channel and shows schematically how we define our turning points. Our approximate solution for $\hat{A}_r$ outside the channel ($r>R_{0,0}$) is given by

$$\hat{A}_r(r,z,t)=\left(\Theta+\frac{1}{4\Theta}\right)^{-1}\frac{A_0}{\sqrt{k_\perp(r)r}}\exp\left[i\int_{R_{0,0}}^{r}k_\perp(r)dr-\frac{(z-v_g t)^2}{\sigma_z^2}+i\delta kz\right], \tag{B3}$$

where A_0 is the amplitude of the mode at the center of the channel and

$$\Theta=\exp\left[-i\int_{r_{0,0}}^{R_{0,0}}k_\perp(r)dr\right]. \tag{B4}$$

The amplitude outside the channel has fallen by a factor of $\Theta+1/4\Theta$. As expected, by extending the evanescent region between $r_{0,0}$ and $R_{0,0}$, Θ becomes larger, limiting the amplitude of outgoing waves. Our expression for the differential radial power loss is then

$$\frac{dP}{dz}=-ck_0\left|\Theta+\frac{1}{4\Theta}\right|^{-2}A_0^2\exp\left[-\frac{2(z-v_g t)^2}{\sigma_z^2}\right]. \tag{B5}$$

The amplitude of the guided mode A_0 will decay as energy leaks out of the channel; in particular, we have that

$$P(z) \simeq \frac{c}{16}(k_0 w_{ch})^2 A_0^2(z). \tag{B6}$$

Inserting Eq. (B6) into Eq. (B5) gives

$$\frac{1}{P}\frac{dP}{dz} = -\frac{16}{k_0 w_{ch}^2}\left|\Theta + \frac{1}{4\Theta}\right|^{-2} \exp\left[-\frac{2(z-v_g t)^2}{\sigma_z^2}\right]. \tag{B7}$$

For simplicity we continue by considering the peak of the pulse and find that $P=P_0 \exp[-z/\zeta]$, where

$$\zeta = \frac{k_0 w_{ch}}{16}\left|\Theta + \frac{1}{4\Theta}\right|^2 w_{ch}. \tag{B8}$$

The leaky channel results in an exponential decay of the guided pulse's power. This decay can be limited by making Θ as large as possible, which is accomplished by using a long flat density profile as shown in Fig. 10(a). Extending the maximum density to a larger radius would also increase the value of Θ, but allows for higher order quasibound modes and may make the guided pulse susceptible to instability as discussed in Appendix A.

APPENDIX C: UNSTABLE SPOT-SIZE OSCILLATIONS

We start by considering solutions to Eq. (2) for a background electron density profile of the form

$$n_e(r,z) = n_0[1+\delta \sin(k_m z)] + \frac{n_0'' r^2}{2}[1+\xi \sin(k_m z)], \tag{C1}$$

which adds a radial profile modulation to Eq. (3). We write the envelope of the transverse vector potential as

$$\hat{A}_r(r,z,t) = A_0(z-v_g t)\frac{r}{w_{ch}}\alpha(z)\exp[-\beta(z)r^2], \tag{C2}$$

where we have used the explicit group velocity approximation explained in the main text, $A_0(z-v_g t)$ determines the pulse shape, $\alpha(z)$ determines the axially dependent phase and amplitude, and $\beta(z)$ determines the axial dependence of the laser spot size. Upon inserting Eq. (C2) into the slowly varying envelope equation we obtain an equation for $\beta(z)$ as follows:

$$\frac{d\beta}{dz} + \frac{2i}{k_0}\beta^2 = \frac{i}{4k_0}\left(\frac{\omega_{p,0}^{2\prime\prime}}{c^2}\right)[1+\xi \sin(k_m z)]. \tag{C3}$$

We expand $\beta=\beta_0+\beta_1+\cdots$, and set the equilibrium value to the matched spot size, $\beta_0=1/w_{ch}^2$. Plugging the expansion into Eq. (C3), we find that β_1 satisfies the equation for a forced harmonic oscillator as follows:

$$\frac{d\beta_1}{dz} + 2i\kappa\beta_1 = \frac{1}{2}i\xi k_0 \kappa^2 \sin(k_m z), \tag{C4}$$

where $\kappa=2/k_0 w_{ch}^2$. When $k_m=2\kappa$, the amplitude of $\beta_1(z)$ will undergo secular growth. In the absence of radial profile modulations, the pulse would undergo spot-size oscillations if it were not matched to the plasma channel, $\beta \neq 1/w_{ch}^2$. The presence of the density profile modulations drives the oscillations resulting in the secular growth. In particular, the solution for $\beta_1(z)$ when $k_m=4/k_0 w_{ch}^2$ is

$$\beta_1(z) = -\frac{\xi}{k_0 w_{ch}^4} z \exp[ik_m z]. \tag{C5}$$

Unstable spot-size oscillations are also possible at higher orders of β due to harmonics of k_m. In general, growth can be expected when $k_m=4/\ell k_0 w_{ch}^2$, where ℓ is an integer. For our parameters, the unstable modulation wavelength is $\lambda_m=(\pi/2)k_0 w_{ch}^2 \sim 0.3$ cm, an order of magnitude higher than the modulation wavelength used. These modulations may be detrimental by spoiling the guiding of a desired mode, or beneficial by spoiling guiding of unwanted modes.

[1] H. M. Milchberg, T. R. Clark, C. G. Durfee III, T. M. Antonsen, Jr., and P. Mora, Phys. Plasmas **3**, 2149 (1996).
[2] H. M. Milchberg, C. G. Durfee III, and T. J. McIlrath, Phys. Rev. Lett. **75**, 2494 (1995).
[3] S. P. D. Mangles *et al.*, Nature (London) **431**, 535–538 (2004).
[4] C. G. R. Geddes *et al.*, Nature (London) **431**, 538–541 (2004).
[5] J. Faure *et al.*, Nature (London) **431**, 541 (2004).
[6] T. Tajima and J. M. Dawson, Phys. Rev. Lett. **43**, 267 (1979).
[7] E. Esarey, P. Sprangle, J. Krall, A. Ting, and G. Joyce, Phys. Fluids B **5**, 2690 (1993).
[8] T. C. Chiou, T. Katsouleas, C. Decker, W. B. Mori, J. S. Wurtele, G. Shvets, and J. J. Su, Phys. Plasmas **2**, 310 (1995).
[9] P. Sprangle, E. Esarey, J. Krall, and G. Joyce, Phys. Rev. Lett. **69**, 2200 (1992).
[10] W. P. Leemans, B. Nagler, A. J. Gonsalves, Cs. Toth, K. Nakamura, C. G. R. Geddes, E. Esarey, C. B. Shroeder, and S. M. Hooker, Nat. Phys. **2**, 696 (2006).
[11] J. D. Lawson, IEEE Trans. Nucl. Sci. **NS-26**, 4217 (1979); P. M. Woodward, J. IEE **93**, 1554 (1947).
[12] P. Sprangle, E. Esarey, and J. Krall, Phys. Plasmas **3**, 2183 (1996).
[13] W. D. Kimura, G. H. Kim, R. D. Romea, L. C. Steinhauer, I. V. Pogorelsky, K. P. Kusche, R. C. Fernow, X. Wang, and Y. Liu, Phys. Rev. Lett. **74**, 546 (1995).
[14] T. Plettner, R. L. Byer, E. Colby, B. Cowan, C. M. S. Sears, J. E. Spencer, and R. H. Siemann, Phys. Rev. Lett. **95**, 134801 (2005).
[15] T. Plettner, R. L. Byer, E. Colby, B. Cowan, C. M. S. Sears, J. E. Spencer, and R. H. Siemann, Phys. Rev. ST Accel. Beams **8**, 121301 (2005).
[16] E. Esarey, P. Sprangle, and J. Krall, Phys. Rev. E **52**, 5443 (1995).
[17] B. Hafizi, A. Ting, E. Esarey, P. Sprangle, and J. Krall, Phys. Rev. E **55**, 5924 (1997).

[18] P. Serafim, P. Sprangle, and B. Hafizi, IEEE Trans. Plasma Sci. **28**, 1190 (2000).
[19] V. Malka, S. Fritzler, E. Lefebvre, M.-M. Aleonard, F. Burgy, J.-P. Chambaret, J.-F. Chemin, K. Krushelnick, G. Malka, S. P. D. Mangles, Z. Najmudin, M. Pittman, J.-P. Rousseau, J.-N. Scheurer, B. Walton, and A. E. Dangor, Science **298**, 1596 (2002).
[20] A. York, B. D. Layer, and H. M. Milchberg, *Advanced Accelerator Concepts*, AIP Conf. Proc. No 877 (AIP, New York, 2006), p. 807.
[21] B. D. Layer, A. York, T. M. Antonsen, S. Varma, Y.-H. Chen, and H. M. Milchberg, Phys. Rev. Lett. **99**, 035001 (2007).
[22] M. Xie, LBNL-48236, "Plasma inverse transition acceleration," 2001.
[23] M. D. Feit and D. E. Maiden, Appl. Phys. Lett. **28**, 331 (1976).
[24] R. Hubbard, P. Sprangle, and B. Hafizi, IEEE Trans. Plasma Sci. **28**, 1159 (2000).
[25] www.glue.umd.edu/~palastro/scatter.mpg
[26] T. M. Antonsen, Jr. and P. Mora, Phys. Rev. Lett. **74**, 4440 (1995).
[27] T. M. Antonsen, Jr. and P. Mora, Phys. Fluids B **5**, 1440 (1993).
[28] P. Mora and T. M. Antonsen, Jr., Phys. Plasmas **4**, 217 (1997).